Monthly patterns of ammonia over the contiguous United States at 2 km resolution

Rui Wang[1], Xuehui Guo[1], Da Pan[1], James T. Kelly[2], Jesse O. Bash[3], Kang Sun[4], Fabien Paulot[5], Lieven Clarisse[6], Martin Van Damme[6], Simon Whitburn[6], Pierre-François Coheur[6], Cathy Clerbaux[6,7], and Mark A. Zondlo[1*]

[1]Department of Civil and Environmental Engineering, Princeton University

[2]Office of Air Quality Planning and Standards, U.S. Environmental Protection Agency, RTP, NC, USA

[3]Office of Research and Development, U.S. Environmental Protection Agency, RTP, NC, USA

[4]Department of Civil, Structural and Environmental Engineering, University at Buffalo, Buffalo, NY, USA

[5]Geophysical Fluid Dynamics Laboratory, National Oceanic and Atmospheric Administration

[6]Université libre de Bruxelles (ULB), Spectroscopy, Quantum Chemistry and Atmospheric Remote Sensing (SQUARES), Brussels, Belgium

[7]Laboratoire Atmosphères, Milieux, Observations Spatiales (LATMOS/IPSL), Sorbonne Université, UVSQ, CNRS, Paris, France

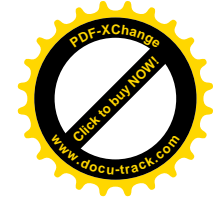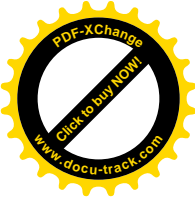Corresponding author: Mark Zondlo (mzondlo@princeton.edu)

Key Points:

- High spatial resolution (2 km) maps of NH_3 show that hotspots are highly localized with characteristic length scales of ~ 12 km.

- Large monthly variations of NH_3 columns are observed with different seasonality patterns by region and type of agricultural activities.

- Satellite NH_3 maps provide insights for future ground-based observational networks and constraints for model NH_3 spatiotemporal patterns.
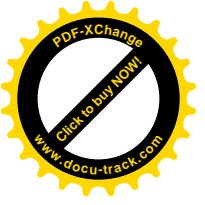
Abstract

Monthly, high resolution (~2 km) ammonia (NH$_3$) column maps from the Infrared Atmospheric Sounding Interferometer (IASI) were developed across the contiguous United States and adjacent areas. Ammonia hotspots (95th percentile of the column distribution) were highly localized with a characteristic length scale of 12 km and median area of 152 km^2. Five seasonality clusters were identified with k-means++ clustering. The Midwest and eastern United States had a broad, spring maximum of NH$_3$ (67% of hotspots in this cluster). The western United States, in contrast, showed a narrower mid-summer peak (32% of hotspots). IASI spatiotemporal clustering was consistent with those from the Ammonia Monitoring Network. CMAQ and GFDL-AM3 modeled NH$_3$ columns have some success replicating the seasonal patterns but did not capture the regional differences. The high spatial-resolution monthly NH$_3$ maps serve as a constraint for model simulations and as a guide for the placement of future, ground-based network sites.
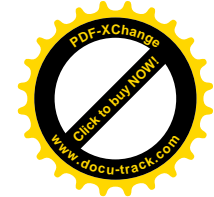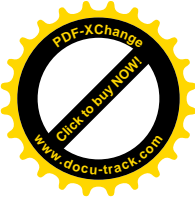
Plain Language Summary

Ammonia (NH$_3$) contributes to the formation of particulate matter, which is known to degrade air quality and human health. The major source of NH$_3$ is from agricultural activities, yet observational constraints on NH$_3$ are limited, particularly at both monthly resolution and high spatial resolution. We have developed high spatial resolution (2 km) satellite maps of NH$_3$ on a monthly scale in the United States. Areas with the highest NH$_3$ are generally very localized with typical length scales of ~ 12 km. The seasonal patterns varied dramatically based upon the underlying agricultural activities. These high-resolution satellite maps can be used as observational constraints on the seasonalities and spatial patterns for modeling of atmospheric NH$_3$.

1 Introduction

Atmospheric ammonia (NH$_3$) affects air quality, climate, and biodiversity through aerosol formation and composition and nitrogen deposition into the biosphere (Hauglustaine et al., 2014; Hill et al., 2019; Li et al., 2016; Malm et al., 2004; Phoenix et al., 2006; Reis et al., 2009). Atmospheric NH$_3$ emissions are principally from agricultural activities, including the volatilization of agricultural waste and fertilizer application in managed croplands (Bouwman et al., 1997; Paulot et al., 2014). Agricultural NH$_3$ emissions significantly degrade air quality with impacts on human health through ammoniated aerosol formation (Hill et al., 2019; Paulot & Jacob, 2014). With respect to climate, ammonium nitrate (NH$_4$NO$_3$) aerosols have a direct radiative forcing of -0.5 W·m^{-2} over the central United States (Hauglustaine et al., 2014) and are increasingly important at the global scale (Paulot et al., 2018).

Despite the recognized importance of NH$_3$, observations of the spatiotemporal variabilities of NH$_3$ are limited, largely due to the extreme difficulties of measuring gas-phase NH$_3$ (von Bobrutzki et al., 2010; Fehsenfeld et al., 2002). The Ammonia Monitoring Network (AMoN) (Puchalski et al., 2015) consists of the only routine measurements of biweekly NH$_3$ across the United States (19 sites in 2010; 107 sites in Jan. 2020). Large differences of NH$_3$

magnitudes and seasonalities exist at short distances between stations (Nair et al., 2019). Satellite NH₃ measurements are now available on a global scale from instruments such as the Infrared Atmospheric Sounding Interferometer (IASI), Cross-track Infrared Sounder (CrIS), Tropospheric Emission Spectrometer (TES), and Atmospheric Infrared Sounder (AIRS) (Clarisse et al., 2009; Shephard et al., 2011; Shephard & Cady-Pereira, 2015; Warner et al., 2016). However, high resolution (~1 km) NH₃ maps have been only provided on an annual basis (Van Damme et al., 2018), or relied on extra meteorological information to perform wind rotation on a point source at a local scale (Clarisse et al., 2019; Dammers et al., 2019). For seasonality studies, the finest spatial resolution was only on the order of $0.1°×0.1°$ (Shephard et al., 2020; Van Damme et al., 2015; Warner et al., 2016), hindering the possibility of identifying small-scale NH₃ hotspots and sub-seasonal variations.

Large discrepancies exist between the chemical transport model predictions of NH₃ and observations on national and regional scales (Battye et al., 2019; Heald et al., 2012; Kelly et al., 2014, 2016, 2018; Nair et al., 2019; Zhu et al., 2013). Bottom-up NH₃ emission inventories require detailed knowledge of spatially- and temporally-resolved farming practices that are rarely available (Paulot et al., 2014; Zhu et al., 2013). From a top-down perspective, Gilliland (2003), Gilliland et al. (2006), Pinder et al. (2006), and Paulot et al. (2014) used NH_x wet deposition data, and Henze et al. (2009) used sulfate and nitrate aerosol compositions to constrain NH₃ emissions magnitude and seasonality, but all studies were limited by the sparse in-situ measurements. Chen et al. (in review) and Zhu et al. (2013) inverted satellite NH₃ observations into NH₃ emissions, but these were conducted at coarse scales (36 – 200 km) and only for three selected months. Cao et al. (2020) performed a 12-month inversion but was still limited by the coarse spatial resolution (~ 30 km) of the chemistry model. The lack of accurate emission inventories results in uncertainties in NH_4NO_3 simulation and hence $PM_{2.5}$ simulation (Holt et al., 2015; Kelly et al., 2018; Walker et al., 2012).

To this end, we have developed monthly, high-resolution $(0.02°×0.02°)$ maps of satellite NH₃ columns over the contiguous United States (CONUS), southern Canada and northern Mexico - together one of the most productive agricultural regions in the world - to better understand NH₃ spatiotemporal variabilities and the characteristics of hotspot regions themselves such as their locations, areas, magnitudes.

2 Methods and Data

The IASI v2.2R retrieval product data (2008-2017) were obtained from the MetOp/A (2008-current) and MetOp/B (2013-current) satellites (limited to cloud fraction ≤10%). Only the morning orbits (equatorial passing time ~ 09:30 local) were analyzed because of higher thermal contrast (sensitivity) versus the evening overpasses (Clarisse et al., 2010). The v2.2R retrieval is based on an artificial neural network for IASI (ANNI) (Whitburn et al., 2016) with the European Centre for Medium-Range Weather Forecasts Re-Analysis (ERA)-Interim reanalysis as its meteorological input (Van Damme et al., 2017). IASI NH₃ observations have been validated on a daily and pixel basis and showed good agreement with in-situ data (Guo et al., in review). A physical-based oversampling approach was used to average the satellite NH₃ observations (level
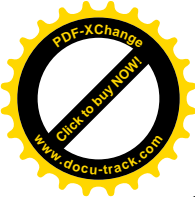
2) to 0.02×0.02° (~ 2 km) grid (level 3) across the CONUS through a generalized 2-D super Gaussian function (Sun et al., 2018). This algorithm weighs IASI measurements by their uncertainties (Sun et al., 2018) which include varying sensitivities to thermal contrast. By using 10-year IASI data, we were able to achieve sufficient overlapped IASI pixels (Text S1 and Figure S1). We focused on the NH_3 intra-annual seasonality and magnitude. Any interannual variability is averaged out, aside from long-term trends of <10% (Yao & Zhang, 2016; Warner et al., 2017), which are generally much smaller than the seasonal variabilities.

For comparisons with models, the Community Multiscale Air Quality (CMAQ) model (version 5.2; www.epa.gov/cmaq) was used with NH_3 emissions from 2014 National Emission Inventory (NEI 2014) for a 2014 simulation on a domain covering CONUS with 12-km horizontal grid resolution (Kelly et al., 2019; US EPA, 2018). The CMAQ simulation included bi-directional air-surface exchange for NH_3 (Bash et al., 2013) based on the resistance parameterization (Massad et al., 2010). We also simulated 0.5×0.5° 2009 - 2013 NH_3 columns by the Geophysical Fluid Dynamics Laboratory (GFDL)-AM3 chemistry-climate model (Donner et al., 2011; Naik et al., 2013; Paulot et al., 2016) using anthropogenic NH_3 emissions from the Community Emissions Data System (CEDS) developed for the Coupled Model Intercomparison Project Phase 6 (CMIP6) (Hoesly et al., 2018). The emissions were monthly distributed according to the ECLIPSE v5 model based on European practices (Friedrich, 2004). Paulot et al. (2017) has a detailed description of the AM3 model configuration. CMAQ and AM3 NH_3 column abundances were obtained at the nearest IASI overpass time. All data over water bodies were excluded. Annual CMAQ and AM3 NH_3 columns are shown in Figure S2 along with their ratios relative to IASI. While key hotspots are broadly consistent with IASI, there remain differences in the areas and absolute and relative magnitudes between the hotspots.

3 Results and Discussion

3.1 High-resolution ammonia annual map

The IASI NH_3 columns were oversampled for each month for all years to get the level 3 oversampled monthly map. Annual maps were made by averaging the monthly maps in equal weights. Figure 1 shows 0.02×0.02° 2008-2017 oversampled NH_3 column abundances derived from IASI observations along with the location of AMoN sites in the CONUS. NH_3 column abundances larger than the 95% percentile (6.6×10^{15} molec·cm^{-2}) of the 10-year averaged level 3 map are defined as "hotspot" regions. This definition of hotspots differs from locating individual emission sources, though these are tightly correlated geographically due to the short lifetime of NH_3. The 95% threshold concentration is not sensitive to the spatial resolution of the oversampling product as coarser resolutions (0.05×0.05°, 0.1×0.1°) have similar 95% percentile values (within ±5%).

By using the Hoshen–Kopelman algorithm to cluster adjacent grid points (Hoshen & Kopelman, 1976) above the 95% threshold, a total of 113 areal hotpots were identified (median area =152 km^2). Detailed hotspots locations and contours are shown in Figure S3. The square root of the median area yielded a characteristic hotspot length scale of 12 km (25th: 8 km, 75th: 24

km). The length scale was fairly insensitive to the oversampling product spatial resolution (0.05×0.05°=13 km; 0.1×0.1°=17 km), increasing slightly as expected due to the coarser grid resolution. The characteristic length scale was insensitive to the percentile as well (90th percentile=5.3 × 10^{15} molec·cm^{-2} yielded 11 km). In general, the characteristic length scale of IASI NH$_3$ hotspots is on the order of 10 km, indicating that coarser resolution (either in model or observations) may miss or average these hotspots into levels more typical of the background.
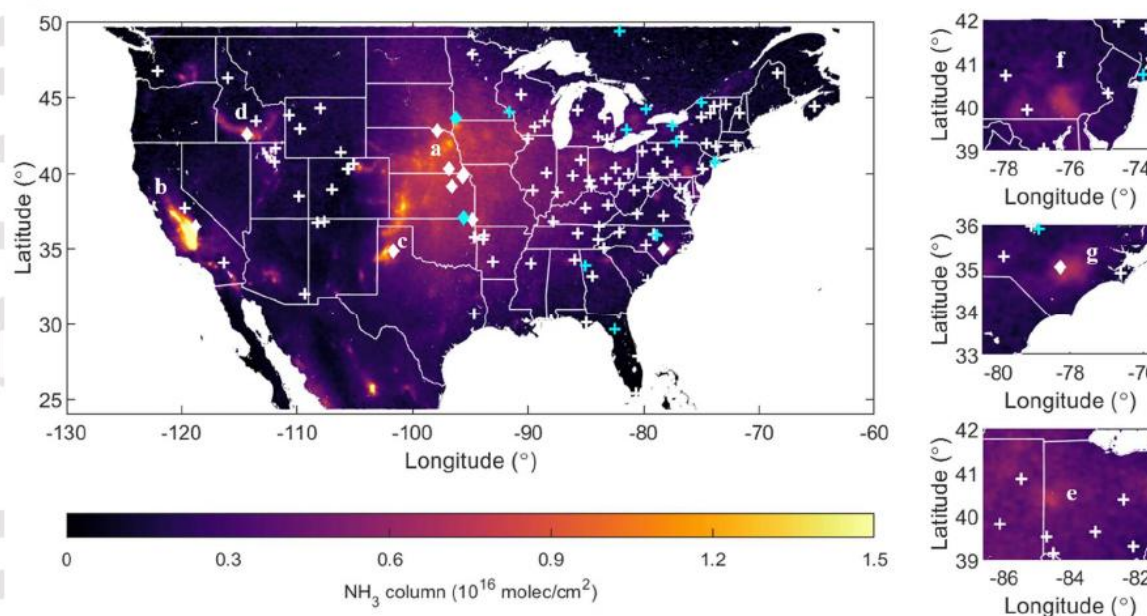

Figure 1. 2008-2017 averaged annual NH$_3$ columns. Each active AMoN site (Jan. 2020) is shown by a diamond "◇" (within 12 km of a hotspot) or a cross "+" symbol. Active AMoN sites are shown in white while inactive sites are shown in cyan. Labeled hotspots are: (a) Great Plains; (b) San Joaquin Valley; (c) Texas panhandle; (d) Snake River Valley (e) west-central Ohio; (f) southeastern Pennsylvania, and (g) eastern North Carolina. For reference, the top 5% of annual NH$_3$ columns ("hotspots") correspond to 0.66×10^{16} molec·cm^{-2}.

The largest contiguous hotspot is in the central Great Plains (386,460 km^2), and the San Joaquin Valley hotspot has the highest annual average column abundance (~ 2.5×10^{16} molec·cm^{-2}). In terms of column-areal weighting, the most important hotspots are the Great Plains, San Joaquin Valley, Texas panhandle, and the Snake River Valley. Although the eastern United States has lower column abundances and fewer hotspot regions than the western United States, PM$_{2.5}$ formation in the eastern United States is more sensitive to NH$_3$ than the western United States (Holt et al., 2015). Important hotspots in the eastern United States include west-central Ohio, southeastern Pennsylvania, and eastern North Carolina. The locations of these high NH$_3$ columns are consistent with those previously reported in-situ observations, satellite analyses, AMoN network, and intensive agricultural activities (Clarisse et al., 2009; Nowak et al., 2012; Schiferl et al., 2014, 2016; Shephard et al., 2011; Van Damme et al., 2018).
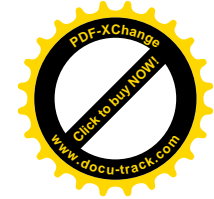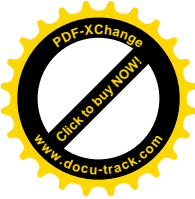
Among the 121 AMoN sites (Figure 1), only 12 AMoN sites are located within 12 km of a hotspot region. AMoN site placement is prioritized to study nitrogen deposition in sensitive ecosystems, and additional sites near hotspots would be valuable for constraining emissions. The high-resolution satellite maps can guide site placement choices in the future, depending upon the ultimate science goal of a site (e.g., emissions vs. downstream deposition).

3.2 Ammonia Seasonality across the CONUS

While annual maps of NH_3 constrain the locations of emission sources, the intra-annual patterns of NH_3 are critical in evaluating aerosol formation and nitrogen deposition. Monthly-averaged maps at a moderate (30-100 km) spatial resolution averages out many hotspots (Van Damme et al., 2014; Warner et al., 2016) and also provides limited information about how different areas evolve during the year. Figure 2 shows the 2008-2017 monthly oversampled NH_3 column concentrations over the CONUS. The general seasonality across the CONUS shows high NH_3 columns in spring/summer, and low NH_3 concentrations in winter, consistent with past studies (Henze et al., 2009; Paulot et al., 2014; Pinder et al., 2006). However, seasonal complexity exists due to regional differences in agricultural practices and climate. NH_3 column maxima are observed in July or August in the western United States, while maxima occur in May/June in the eastern United States (Figure S4 in SI), in broad agreement with past work at coarser resolution (Van Damme et al., 2015).

The differences in monthly NH_3 patterns are partially attributed to the dominant agricultural land use types for each region. The western United States is dominated by pasture lands (USDA, 2017), and the livestock waste volatilizes to produce NH_3 with increasing temperatures (Gyldenkærne et al., 2005). The eastern United States is featured by both pasture lands and croplands (USDA, 2017), and fertilizer and manure emissions lead to complex patterns across spring, summer, and fall. Note that the absolute differences between the monthly maxima and minima are large - on the order of 10^{16} molec·cm^{-2} - for most of the hotspot regions (Fig. S5 in SI).
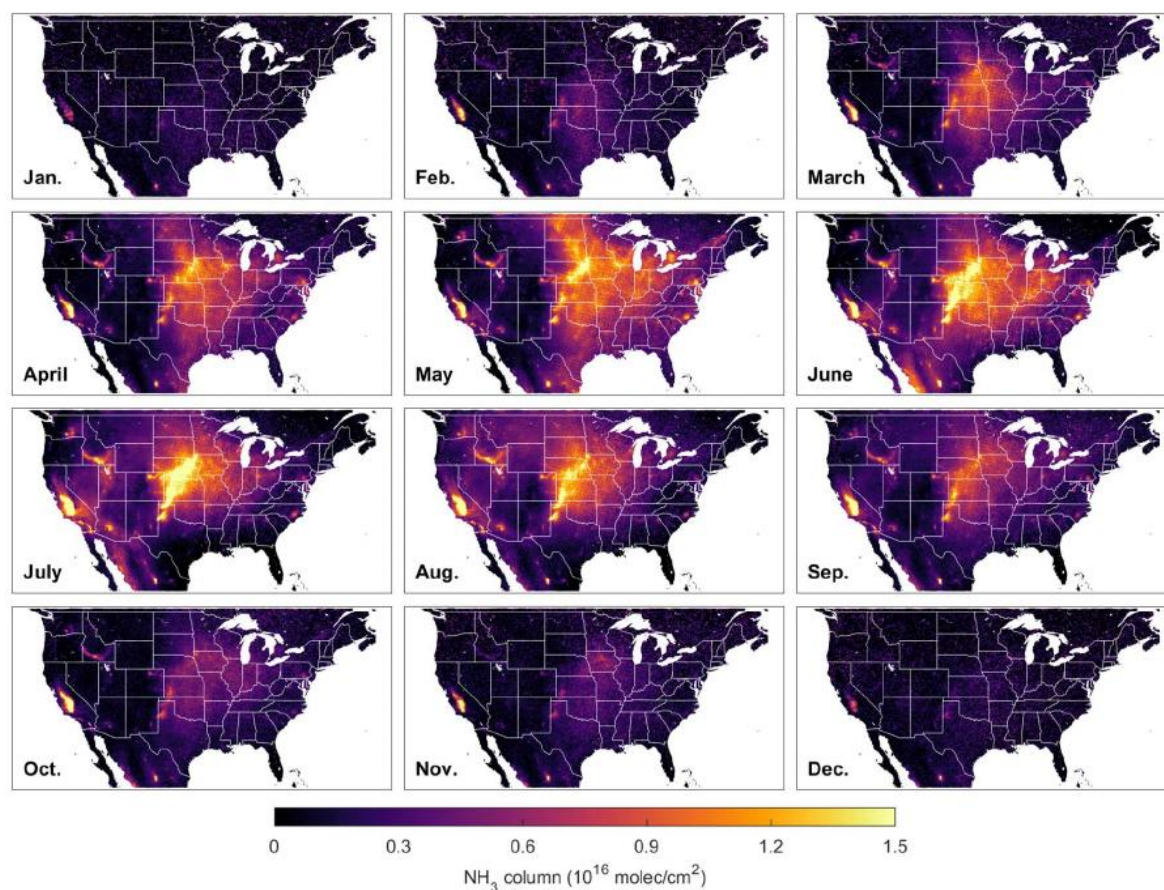
Figure 2. IASI 2008-2017 oversampled NH_3 column concentration over CONUS from January to December.

To better understand the NH_3 seasonal patterns beyond the monthly maxima, the IASI NH_3 seasonality was examined using k-means++ clustering (Forgy, 1965; Arthur & Vassilvitskii, 2007) of the monthly IASI NH_3 columns. As an unsupervised learning algorithm, k-means++ groups observations so that the average squared distance between data in the same cluster is minimized (Forgy, 1965; Arthur & Vassilvitskii, 2007). The advantage of applying k-means clustering is the lack of any *a-priori* assumption of regional seasonality. The data defines the geographical regions that have similar seasonality, and k-means++ is independently performed on different datasets. Monthly NH_3 data were standardized to have a mean of 0 and a variance of 1. Therefore, the clustering is not affected by differences in the mean or variance but is instead based on the correlation among all standardized monthly concentrations (Zhang et al., 2016). Because the optimal number of clusters is influenced by the underlying data and its patterns (Text S2 in SI), different optimal numbers of clusters were identified for each dataset (e.g., IASI, AMoN, model products).

Figure 3 shows the five geographic clusters (3a) identified for IASI NH_3 and their seasonal dependencies (3b). The area from Central Plains to the Great Lakes resides in a cluster

with a broad, May peak, and a secondary shoulder in September (cluster 1). To the southeast of that area across the South and along the Gulf Coast (cluster 2), there is a peak in May, a local minimum in July, and a secondary smaller peak in September/October. The interior western U.S. and adjacent high plains are subdivided into a narrower and more pronounced peak in July for the southwest (cluster 3) or August for the northwest (cluster 4). New England, boreal Ontario, and Québec, and the maritime provinces (cluster 5) have relatively small variations all year round.

Springtime maxima are consistent with the timing of fertilizer application, particularly the later start of the growing season as one moves northward (USDA, 2010). Fall maxima or shoulders are also consistent with fall-based fertilizer application (Goebes et al., 2003; USDA, 2010). In contrast, the narrower, summer peaks of the western United States and high plains are more consistent with the volatilization of livestock waste that strongly correlates with maximum air temperatures (Gyldenkærne et al., 2005). Feedlots and croplands are often adjacent to one another, making definitive agricultural use classifications difficult. Most hotspot regions (67%) fall into the group with a broad peak from spring to early fall (cluster 1), indicating contributions from both livestock waste and fertilizer application. The remainder (32%) fall into one of the two clusters (3 and 4) with the sharp, summer peaks associated more closely with feedlot emissions. Besides agricultural emissions, biomass burning may also contribute to some of the seasonality (Bouwman et al., 1997), especially in summer in the western United States and agricultural burning in the fall in the southeastern United States (Bray et al., 2018; Giglio et al., 2006; Luo et al., 2015).

Figure 3 also shows CMAQ (c, d) and AM3 (e, f) modeled NH_3 seasonality clusters using k-means++. The clusters of CMAQ range from a strong summer peak (cluster i) to bimodal peaks in spring and fall (cluster ii). The differences between the CMAQ clusters fall within a narrower range than the differences among the observed IASI clusters. All AM3 clusters show bimodal peaks in spring and fall with varying relative magnitudes. The geographic locations of the model NH_3 clusters are far more random and less consistent geographically with their neighbors than the IASI clusters (cf. Figure S6 shows CMAQ and AM3 seasonalities averaged to the IASI spatial clusters). Overall, the temporal evolution of the key clusters in AM3 and CMAQ shows agreement with IASI seasonality clusters, but the spatial patterns of the CMAQ and AM3 clusters strongly differ from those of IASI.

K-means++ clustering was also applied to the much smaller AMoN dataset. Three seasonality clusters were identified for 104 AMoN sites with sufficient (≥1-year record) seasonality measurements as shown in Figure 3 (g, h). Cluster γ, covering most of the eastern and Midwest U.S. sites, has a broad, single peak in June. Cluster α is featured by a peak in July and covers most regions in the western United States, in good agreement with the seasonal pattern classification with IASI. Cluster β shows a relatively insignificant seasonal variability except for a peak in November that is associated with 7 sites and may be related to influences from unidentified local sources. IASI and AMoN patterns are not perfectly matched, but both show the similar spatial clusters of seasonalities between the western and Midwestern/eastern United States and also are broadly consistent on the NH_3 seasonalities for each geographic area.
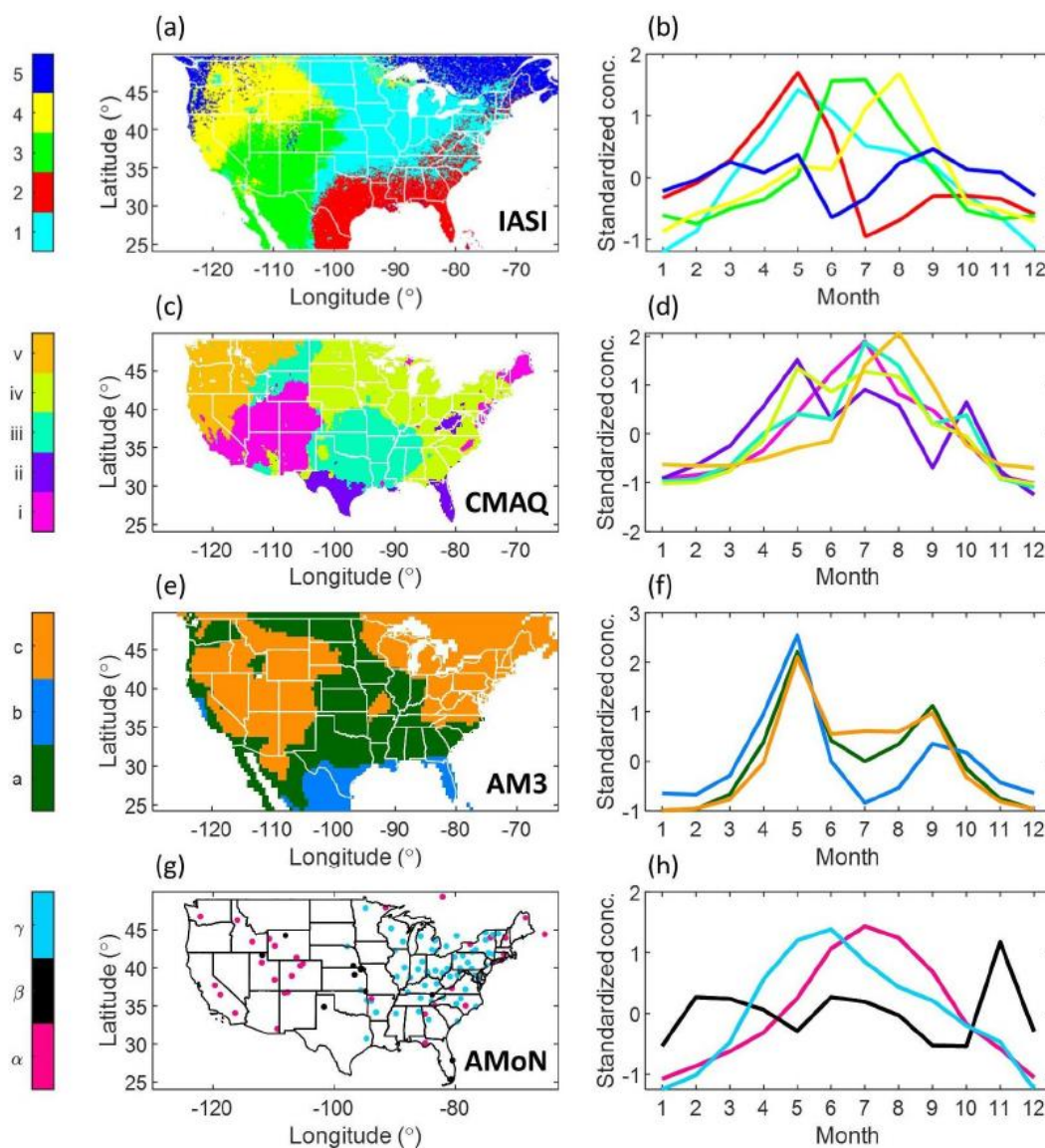
Figure 3. IASI, CMAQ, AM3, and AMoN NH$_3$ seasonality clusters map (a) (c) (e) (g) and standardized NH$_3$ concentrations for each cluster (b) (d) (f) (h).

The patterns of IASI and modeled NH$_3$ seasonality are affected by many factors such as emissions, partitioning, and deposition. With respect to aerosol partitioning, gas-phase NH$_3$ compromises much of the total NH$_x$ in the warm season for both models (Figure S7, S8). For deposition, only a small fraction (5-15%) dry deposits within 15 km (Dennis et al., 2010; Miller et al., 2015). Indeed, Nair et al. (2019) showed that the modeled NH$_3$ concentrations have a strong spatial dependence on NH$_3$ emissions. However, away from hotspots and during the cold

season, deposition and partitioning likely become more important contributors to the seasonal patterns than the underlying emission inventory. Because CMAQ and AM3 modeling results are based on state or county level emission inventory statistics, satellite observations constraints can be used to ameliorate the effects of these geopolitical boundaries on model output.

3.3 Seasonality of hotspots: comparison of model and observations

Case studies of IASI and AMoN NH_3 seasonality over hotspots were examined and compared to CMAQ and AM3 columns. Three 0.5 × 0.5 ° hotspot subregions were selected for comparison: 1) central Tulare County, California, the location of the highest IASI NH_3 column (3.2×10^{16} molec·cm^{-2}) composed of 58% cropland, 36% pastureland (USDA, 2017); 2) Cache County, Utah, the location of the highest annual AMoN NH_3 surface concentrations (~ 15 μg/m^3) in the network (58% cropland, 37% pastureland, USDA, 2017); and 3) Jo Daviess County, Illinois, a more cropland dominated hotspot (70% cropland, 14% pastureland) (USDA, 2017). Figures 4 (a) (c) (e) show the IASI oversampled NH_3 column concentrations in Tulare, Cache, and Jo Daviess counties, respectively. Fig. 4 (b) (d) (f) show the corresponding seasonality comparison between IASI, CMAQ, AM3 NH_3 columns, and AMoN NH_3 surface concentration. While the years included for AMoN, IASI, and model results differed amongst themselves at each site, the interannual variabilities are expected to be averaged out (Figure S9).

The three hotspots display distinctly different IASI NH_3 seasonalities, showing that hotspot regions cannot be treated identically. For Tulare County, IASI, AMoN, and CMAQ all show a broad summer peak in Tulare County, while AM3 shows a bimodal peak. For Cache County, all four patterns differ between AMoN, IASI, CMAQ, and AM3. AMoN measures a relatively flat pattern across the year, IASI shows a broad spring peak, CMAQ has a stronger summer peak, and AM3 has bimodal peaks. While IASI identifies Cache County as a hotspot, the AMoN site has the highest annual average in the CONUS. However, this AMoN site is only ~ 100 m away from feedlots, a distance in which concentrations are strongly enhanced relative to background levels (Miller et al., 2015; Golston et al., 2020). There are also intrinsic differences between a surface concentration and column amount that complicate comparisons between IASI and AMoN (e.g., boundary layer height). Meanwhile, Jo Daviess County exhibits a broad spring peak in IASI, but a bimodal structure in AMoN and AM3. IASI NH_3 columns over hotspot regions allow one to test the relevant model parameters that impact seasonality (e.g., partitioning, emissions, deposition, transport).
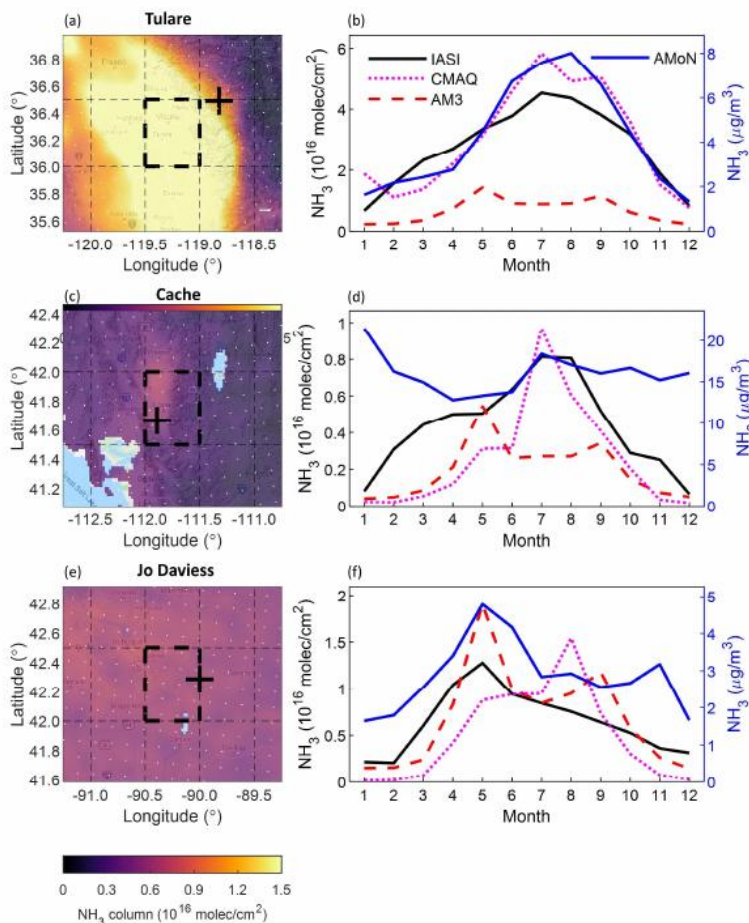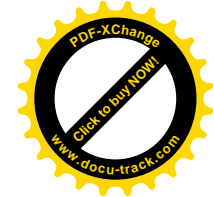
Figure 4. Comparison of NH₃ seasonality in hotspots regions. Panels (a) (c) (e) are the annual averaged IASI oversampled NH₃ column concentrations. The bold black dashed box indicates the selected hotspot regions. The black cross shows the nearby AMoN site. Black dashed lines represent AM3 grid boxes, and white dots represent the center of CMAQ grids. (b) (d) (f) are the NH₃ seasonality derived from the IASI oversampling NH₃ column, CMAQ and AM3 modeled NH₃ columns (left axis), and AMoN NH₃ concentration (right axis). Map data from Google Earth.

4 Implications

Ammonia columns near source regions are very localized (~ 12 km scale) and with strong spatial gradients. Because NH₃ hotspots have a strong influence on the air quality and nitrogen deposition in nearby regions (Benedict et al., 2013), there is an urgent need to understand processes such as the underlying spatial pattern of emission inventories, deposition, transport, and partitioning at these same scales. Satellite data may help improve future site placement depending upon the desired objective (e.g., investigating hotspots emissions or characterizing downwind deposition). Ultimately, the differences in spatial and temporal scales between

satellite observations (an instantaneous volume) and AMoN (two-week point measurement) require careful attention to many factors for robust comparisons (Kharol et al., 2018).

At monthly scales, the high-resolution NH_3 maps provide improved, observational-based means to help constrain NH_3 seasonality for improved regional scale modeling of $PM_{2.5}$ and deposition. The differences between satellite and modeled NH_3 seasonal patterns, especially for the global emission inventories developed for CMIP6, further demonstrate the importance of evaluating modeled NH_3 with satellite measurements. Simply using the annual averages with *a priori* seasonalities applied is not accurate. To this end, recent work by Chen et al. (in review) is promising where IASI NH_3 is inverted at 36 km resolution for April, July, and October with much different emissions spatially and temporally. Accurate modeling of boundary layer height, vertical profiles of temperature, humidity, and NH_3 within the boundary layer, aerosol partitioning, and chemical lifetime are all needed to fully transform these column maps into accurate spatiotemporal emission inventories. Finally, improved validation of satellite-derived NH_3 columns is also needed to reduce biases at these scales (especially for conditions of temperature inversions during winter and in valleys).
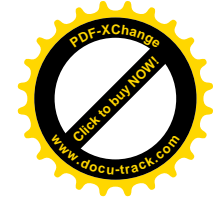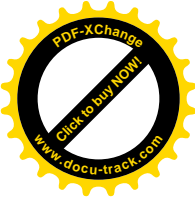
Acknowledgments

Data availability

The monthly resolved 0.02×0.02° IASI oversampling data, IASI data animations, and kmz file of annual data are available on the persistent URL: https://dataspace.princeton.edu/handle/88435/dsp018s45qc83f, DOI: https://doi.org/10.34770/J1Q6-2Y79.

References

Arthur, D., and S. Vassilvitskii (2007). K-means++: The advantages of careful seeding. Paper presented at *In Proceedings of the eighteenth annual ACM-SIAM symposium on Discrete algorithms (SODA '07). Society for Industrial and Applied Mathematics,* New Orleans, Louisiana

Bash, J. O., Cooter, E. J., Dennis, R. L., Walker, J. T., & Pleim, J. E. (2013). Evaluation of a regional air-quality model with bidirectional NH_3 exchange coupled to an agroecosystem model. *Biogeosciences*, *10*(3), 1635–1645. https://doi.org/10.5194/bg-10-1635-2013

Battye, W. H., Bray, C. D., Aneja, V. P., Tong, D., Lee, P., & Tang, Y. (2019). Evaluating

Ammonia (NH₃) Predictions in the NOAA NAQFC for Eastern North Carolina Using Ground Level and Satellite Measurements. *Journal of Geophysical Research: Atmospheres*, *124*(14), 8242–8259. https://doi.org/10.1029/2018JD029990

Benedict, K. B., Day, D., Schwandner, F. M., Kreidenweis, S. M., Schichtel, B., Malm, W. C., & Collett, J. L. (2013). Observations of atmospheric reactive nitrogen species in Rocky Mountain National Park and across northern Colorado. *Atmospheric Environment*, *64*, 66–76. https://doi.org/10.1016/j.atmosenv.2012.08.066

von Bobrutzki, K., Braban, C. F., Famulari, D., Jones, S. K., Blackall, T., Smith, T. E. L., et al. (2010). Field inter-comparison of eleven atmospheric ammonia measurement techniques. *Atmospheric Measurement Techniques*, *3*, 91–112. https://doi.org/10.5194/amt-3-91-2010

Bouwman, A. F., Lee, D. S., Asman, W. A. H., Dentener, F. J., Van Der Hoek, K. W., & Olivier, J. G. J. (1997). A global high-resolution emission inventory for ammonia. *Global Biogeochemical Cycles*, *11*(4), 561–587. https://doi.org/10.1029/97GB02266

Bray, C. D., Battye, W., Aneja, V. P., Tong, D. Q., Lee, P., & Tang, Y. (2018). Ammonia emissions from biomass burning in the continental United States. *Atmospheric Environment*, *187*, 50–61. https://doi.org/10.1016/j.atmosenv.2018.05.052

Cao, H., Henze, D. K., Shephard, M. W., Dammers, E., Cady-Pereira, K., Alvarado, M., et al. (2020). Inverse modeling of NH₃ sources using CrIS remote sensing measurements . *Environmental Research Letters*, *15*(10), 104082. https://doi.org/10.1088/1748-9326/abb5cc

Chen, Y., Shen, H., Kaiser, J., Hu, Y., Capps, S. L., Zhao, S., et al. (2020): High-resolution Hybrid Inversion of IASI Ammonia Columns to Constrain U.S. Ammonia Emissions Using the CMAQ Adjoint Model. *Atmospheric Chemistry and Physics Discussion*, https://doi.org/10.5194/acp-2020-523, in review

Clarisse, L., Clerbaux, C., Dentener, F., Hurtmans, D., & Coheur, P.-F. (2009). Global ammonia distribution derived from infrared satellite observations. *Nature Geoscience*, *2*(7), 479–483. https://doi.org/10.1038/ngeo551

Clarisse, L., Shephard, M. W., Dentener, F., Hurtmans, D., Cady-Pereira, K., Karagulian, F., et al. (2010). Satellite monitoring of ammonia: A case study of the San Joaquin Valley. *Journal of Geophysical Research: Atmosphere*, *115*(D13), D13302. https://doi.org/10.1029/2009JD013291

Clarisse, L., Van Damme, M., Clerbaux, C., & Coheur, P. F. (2019). Tracking down global NH₃ point sources with wind-adjusted superresolution. *Atmospheric Measurement Techniques*, *12*(10), 5457–5473. https://doi.org/10.5194/amt-12-5457-2019

Dennis, R. L., Mathur, R., Pleim, J. E., & Walker, J. T. (2010). Fate of ammonia emissions at the local to regional scale as simulated by the Community Multiscale Air Quality model. *Atmospheric Pollution Research*, *1*(4), 207–214. https://doi.org/10.5094/APR.2010.027

Donner, L. J., Wyman, B. L., Hemler, R. S., Horowitz, L. W., Ming, Y., Zhao, M., et al. (2011). The dynamical core, physical parameterizations, and basic simulation characteristics of the atmospheric component AM3 of the GFDL global coupled model CM3. *Journal of Climate*, *24*(13), 3484–3519. https://doi.org/10.1175/2011JCLI3955.1

Fehsenfeld, F. C., Huey, L. G., Leibrock, E., Dissly, R., Williams, E., Ryerson, T. B., et al.

(2002). Results from an informal intercomparison of ammonia measurement techniques. *Journal of Geophysical Research: Atmospheres*. *107*(D24), ACH–28. https://doi.org/10.1029/2001JD001327

Forgy, E. (1965). Cluster analysis of multivariate data : efficiency versus interpretability of classifications. *Biometrics*. *21*, 768–869.

Friedrich, R., and Reis, S. (2004), *Emissions of Air Pollutants: Measurements, Calculations and Uncertainties*, Springer, Berlin Heidelberg, New York.Giglio, L., Csiszar, I., & Justice, C. O. (2006). Global distribution and seasonality of active fires as observed with the Terra and Aqua Moderate Resolution Imaging Spectroradiometer (MODIS) sensors. *Journal of Geophysical Research: Biogeosciences*, *111*(2), 1–12. https://doi.org/10.1029/2005JG000142

Gilliland, A. B. (2003). Seasonal NH_3 emission estimates for the eastern United States based on ammonium wet concentrations and an inverse modeling method. *Journal of Geophysical Research*, *108*(D15), 4477. https://doi.org/10.1029/2002JD003063

Gilliland, A. B., Wyat Appel, K., Pinder, R. W., & Dennis, R. L. (2006). Seasonal NH_3 emissions for the continental united states: Inverse model estimation and evaluation. *Atmospheric Environment*, *40*(26), 4986–4998. https://doi.org/10.1016/j.atmosenv.2005.12.066

Goebes, M. D., Strader, R., & Davidson, C. (2003). An ammonia emission inventory for fertilizer application in the United States. *Atmospheric Environment*, *37*(18), 2539–2550. https://doi.org/10.1016/S1352-2310(03)00129-8

Golston, L. M., Pan, D., Sun, K., Tao, L., Zondlo, M. A., et al., (2020). Variability of ammonia and methane emissions from animal feeding operations in northeastern Colorado. *Environmental Science & Technology*. https://doi.org/10.1021/acs.est.0c00301

Guo, X. G., Clarisse, L., Wang, R., Van Damme, M., Whitburn, S., Coheur, P. F., et al. Validation of IASI satellite ammonia observations at the pixel scale using in-situ vertical profiles. *Journal of Geophysical Research: Atmospheres*, in review

Gyldenkærne, S., Skjøth, C. A., Hertel, O., & Ellermann, T. (2005). A dynamical ammonia emission parameterization for use in air pollution models. *Journal of Geophysical Research: Atmospheres*, *110*(7), 1–14. https://doi.org/10.1029/2004JD005459

Hauglustaine, D. A., Balkanski, Y., & Schulz, M. (2014). A global model simulation of present and future nitrate aerosols and their direct radiative forcing of climate. *Atmospheric Chemistry and Physics*, *14*(20), 11031–11063. https://doi.org/10.5194/acp-14-11031-2014

Heald, C. L., Collett, J. L., Lee, T., Benedict, K. B., Schwandner, F. M., Li, Y., et al. (2012). Atmospheric ammonia and particulate inorganic nitrogen over the United States. *Atmospheric Chemistry and Physics*, *12*(21), 10295–10312. https://doi.org/10.5194/acp-12-10295-2012

Henze, D. K., Seinfeld, J. H., & Shindell, D. T. (2009). Inverse modeling and mapping US air quality influences of inorganic PM 2.5 precursor emissions using the adjoint of GEOS-Chem. *Atmospheric Chemistry and Physics*. https://doi.org/10.5194/acp-9-5877-2009

Hill, J., Goodkind, A., Tessum, C., Thakrar, S., Tilman, D., Polasky, S., et al. (2019). Air-

quality-related health damages of maize. *Nature Sustainability*, *2*(5), 397–403. https://doi.org/10.1038/s41893-019-0261-y

Hoesly, R. M., Smith, S. J., Feng, L., Klimont, Z., Janssens-Maenhout, G., Pitkanen, T., et al. (2018). Historical (1750-2014) anthropogenic emissions of reactive gases and aerosols from the Community Emissions Data System (CEDS). *Geoscientific Model Development*. https://doi.org/10.5194/gmd-11-369-2018

Holt, J., Selin, N. E., & Solomon, S. (2015). Changes in inorganic fine particulate matter sensitivities to precursors due to large-scale us emissions reductions. *Environmental Science and Technology*, *49*(8), 4834–4841. https://doi.org/10.1021/acs.est.5b00008

Hoshen, J., & Kopelman, R. (1976). Percolation and cluster distribution. I. Cluster multiple labeling technique and critical concentration algorithm. *Physical Review B.* https://doi.org/10.1103/PhysRevB.14.3438

Kelly, J. T., Baker, K. R., Nowak, J. B., Murphy, J. G., Markovic, M. Z., Vandenboer, T. C., et al. (2014). Fine-scale simulation of ammonium and nitrate over the south coast air basin and san joaquin valley of California during CalNex-2010. *Journal of Geophysical Research: Atmospheres, 119*(6): 3600-3614. https://doi.org/10.1002/2013JD021290

Kelly, J. T., Baker, K. R., Nolte, C. G., Napelenok, S. L., Keene, W. C., & Pszenny, A. A. P. (2016). Simulating the phase partitioning of NH_3, HNO_3, and HCl with size-resolved particles over northern Colorado in winter. *Atmospheric Environment*, *131*, 67–77. https://doi.org/10.1016/j.atmosenv.2016.01.049

Kelly, J. T., Parworth, C. L., Zhang, Q., Miller, D. J., Sun, K., Zondlo, M. A., et al. (2018). Modeling NH_4NO_3 Over the San Joaquin Valley During the 2013 DISCOVER-AQ Campaign. *Journal of Geophysical Research: Atmospheres*, *123*(9), 4727–4745. https://doi.org/10.1029/2018JD028290
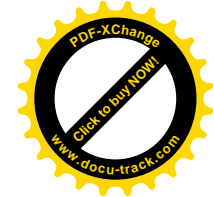
Kelly, J. T., Koplitz, S. N., Baker, K. R., Holder, A. L., Pye, H. O. T., Murphy, B. N., et al. (2019). Assessing $PM_{2.5}$ model performance for the conterminous U.S. with comparison to model performance statistics from 2007-2015. *Atmospheric Environment*, *214*, 116872. https://doi.org/10.1016/j.atmosenv.2019.116872

Kharol, S. K., Shephard, M. W., McLinden, C. A., Zhang, L., Sioris, C. E., O'Brien, J. M., et al. (2018). Dry deposition of reactive nitrogen from satellite observations of ammonia and nitrogen dioxide over North America. *Geophysical Research Letters*. https://doi.org/10.1002/2017GL075832

Li, Y., Schichtel, B. A., Walker, J. T., Schwede, D. B., Chen, X., Lehmann, C. M. B., et al. (2016). Increasing importance of deposition of reduced nitrogen in the United States. *Proceedings of the National Academy of Sciences*, *113*(21), 5874–5879.
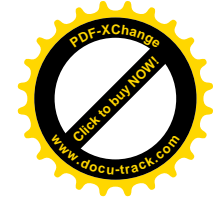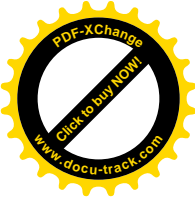
Luo, M., Shephard, M. W., Cady-Pereira, K. E., Henze, D. K., Zhu, L., Bash, J. O., et al. (2015). Satellite observations of tropospheric ammonia and carbon monoxide: Global distributions, regional correlations and comparisons to model simulations. *Atmospheric Environment*, *106*, 262–277. https://doi.org/10.1016/j.atmosenv.2015.02.007

Malm, W. C., Schichtel, B. A., Pitchford, M. L., Ashbaugh, L. L., & Eldred, R. A. (2004). Spatial and monthly trends in speciated fine particle concentration in the United States. *Journal of Geophysical Research: Atmospheres*, *109*(D3), D03306.

https://doi.org/10.1029/2003JD003739

Massad, R. S., Nemitz, E., & Sutton, M. A. (2010). Review and parameterisation of bi-directional ammonia exchange between vegetation and the atmosphere. *Atmospheric Chemistry and Physics*, *10*(21), 10359–10386. https://doi.org/10.5194/acp-10-10359-2010

Miller, D. J., Sun, K., Tao, L., Pan, D., Zondlo, M. A., Nowak, J. B., et al. (2015). Ammonia and methane dairy emission plumes in the San Joaquin valley of California from individual feedlot to regional scales. *Journal of Geophysical Research: Atmospheres*, *120*(18), 9718–9738. https://doi.org/10.1002/2015JD023241

Naik, V., Voulgarakis, A., Fiore, A. M., Horowitz, L. W., Lamarque, J. F., Lin, M., et al. (2013). Preindustrial to present-day changes in tropospheric hydroxyl radical and methane lifetime from the Atmospheric Chemistry and Climate Model Intercomparison Project (ACCMIP). *Atmospheric Chemistry and Physics*, *13*(10), 5277–5298. https://doi.org/10.5194/acp-13-5277-2013

Nair, A. A., Yu, F., & Luo, G. (2019). Spatioseasonal Variations of Atmospheric Ammonia Concentrations Over the United States: Comprehensive Model-Observation Comparison. *Journal of Geophysical Research: Atmospheres*, *124*(12), 6571–6582. https://doi.org/10.1029/2018JD030057

National Atmospheric Deposition Program (NRSP-3) (2020). NADP Program Office, Wisconsin State Laboratory of Hygiene, Madison, WI. Available: http://nadp.slh.wisc.edu/AMoN/

Nowak, J. B., Neuman, J. A., Bahreini, R., Middlebrook, A. M., Holloway, J. S., McKeen, S. A., et al. (2012). Ammonia sources in the California South Coast Air Basin and their impact on ammonium nitrate formation. *Geophysical Research Letters*, *39*(7), 6–11. https://doi.org/10.1029/2012GL051197

Paulot, F., Jacob, D. J., Pinder, R. W., Bash, J. O., Travis, K., & Henze, D. K. (2014). Ammonia emissions in the United States, european union, and China derived by high-resolution inversion of ammonium wet deposition data: Interpretation with a new agricultural emissions inventory (MASAGE_NH3). *Journal of Geophysical Research: Atmospheres*, *119*(7), 4343–4364. https://doi.org/10.1002/2013JD021130

Paulot, F., Ginoux, P., Cooke, W. F., Donner, L. J., Fan, S., Lin, M. Y., et al. (2016). Sensitivity of nitrate aerosols to ammonia emissions and to nitrate chemistry: Implications for present and future nitrate optical depth. *Atmospheric Chemistry and Physics*, *16*(3), 1459–1477. https://doi.org/10.5194/acp-16-1459-2016

Paulot, F., Paynter, D., Ginoux, P., Naik, V., Whitburn, S., Van Damme, M., et al. (2017). Gas-aerosol partitioning of ammonia in biomass burning plumes: Implications for the interpretation of spaceborne observations of ammonia and the radiative forcing of ammonium nitrate. *Geophysical Research Letters*, *44*(15), 8084–8093. https://doi.org/10.1002/2017GL074215

Paulot, F., & Jacob, D. J. (2014). Hidden cost of U.S. agricultural exports: Particulate matter from ammonia emissions. *Environmental Science and Technology*, *48*(2), 903–908. https://doi.org/10.1021/es4034793

Paulot, F., Paynter, D., Ginoux, P., Naik, V., & Horowitz, L. W. (2018). Changes in the aerosol direct radiative forcing from 2001 to 2015: Observational constraints and regional

mechanisms. *Atmospheric Chemistry and Physics*, *18*(17), 13265–13281. https://doi.org/10.5194/acp-18-13265-2018

Phoenix, G. K., Hicks, W. K., Cinderby, S., Kuylenstierna, J. C. I., Stock, W. D., Dentener, F. J., et al. (2006). Atmospheric nitrogen deposition in world biodiversity hotspots: The need for a greater global perspective in assessing N deposition impacts. *Global Change Biology*, *12*(3), 470–476. https://doi.org/10.1111/j.1365-2486.2006.01104.x

Pinder, R. W., Adams, P. J., Pandis, S. N., & Gilliland, A. B. (2006). Temporally resolved ammonia emission inventories: Current estimates, evaluation tools, and measurement needs. *Journal of Geophysical Research: Atmospheres*, *111*(16). https://doi.org/10.1029/2005JD006603

Puchalski, M. A., Rogers, C. M., Baumgardner, R., Mishoe, K. P., Price, G., Smith, M. J., et al. (2015). A statistical comparison of active and passive ammonia measurements collected at Clean Air Status and Trends Network (CASTNET) sites. *Environmental Sciences: Processes and Impacts*. https://doi.org/10.1039/c4em00531g

Reis, S., Pinder, R. W., Zhang, M., Lijie, G., & Sutton, M. A. (2009). Reactive nitrogen in atmospheric emission inventories. *Atmospheric Chemistry and Physics*, *9*, 7657–7677. https://doi.org/10.5194/acp-9-7657-2009, 2009

Schiferl, L. D., Heald, C. L., Nowak, J. B., Holloway, J. S., Neuman, J. A., Bahreini, R., et al. (2014). An investigation of ammonia and inorganic particulate matter in california during the CalNex campaign. *Journal of Geophysical Research: Atmospheres*. *119*(4), 1883-1902. https://doi.org/10.1002/2013JD020765

Schiferl, L. D., Heald, C. L., Damme, M. Van, Clarisse, L., Clerbaux, C., Coheur, P., et al. (2016). Interannual variability of ammonia concentrations over the United States : sources and implications. *Atmospheric Chemistry and Physics*, *16*, 12305–12328. https://doi.org/10.5194/acp-16-12305-2016

Seinfeld, J. H., & Pandis, S. N. (2016). *Atmospheric Chemistry and Physics: From Air Pollution to Climate Change*, 3rd Edition. Hoboken, NJ: John Wiley & Sons.

Shephard, M. W., Cady-Pereira, K. E., Luo, M., Henze, D. K., Pinder, R. W., Walker, J. T., et al. (2011). TES ammonia retrieval strategy and global observations of the spatial and seasonal variability of ammonia. *Atmospheric Chemistry and Physics*, *11*(20), 10743–10763. https://doi.org/10.5194/acp-11-10743-2011
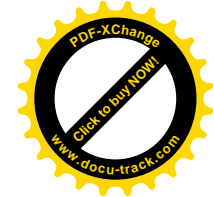
Shephard, M. W., & Cady-Pereira, K. E. (2015). Cross-track Infrared Sounder (CrIS) satellite observations of tropospheric ammonia. *Atmospheric Measurement Techniques*, *8*(3), 1323–1336. https://doi.org/10.5194/amt-8-1323-2015

Shephard, M. W., Dammers, E., Cady-Pereira, K. E., Kharol, S. K., Thompson, J., Gainariu-Matz, et al. (2020). Ammonia measurements from space with the Cross-track Infrared Sounder: characteristics and applications, *Atmospheric Chemistry and Physic*, 20, 2277–2302, https://doi.org/10.5194/acp-20-2277-2020, 2020

Sun, K., Zhu, L., Cady-Pereira, K., Chan Miller, C., Chance, K., Clarisse, L., et al. (2018). A physics-based approach to oversample multi-satellite, multispecies observations to a common grid. *Atmospheric Measurement Techniques*, *11*(12), 6679–6701. https://doi.org/10.5194/amt-11-6679-2018
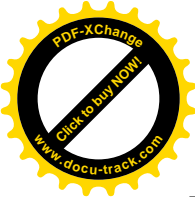
USDA National Agricultural Statistics Service (2010). Field Crops Usual Planting and Harvesting Dates. Available: https://www.nass.usda.gov/Publications/Todays_Reports/reports/fcdate10.pdf

USDA National Agricultural Statistics Service (2017). Census of Agriculture. Available: https://www.nass.usda.gov/AgCensus

USDA National Agricultural Statistics Service (2020). Cropland Data Layer. Published crop-specific data layer [Online]. USDA-NASS, Washington, DC. Available: https://nassgeodata.gmu.edu/CropScape/

USEPA (2018). Bayesian space-time downscaling fusion model (downscaler) -Derived Estimates of Air Quality for 2014. U.S. Environmental Protection Agency, Office of Air Quality Planning and Standards, Research Triangle Park, NC. EPA-454/R-18-008 Available: https://www.epa.gov/hesc/rsig-related-downloadable-data-files

Van Damme, M., Clarisse, L., Heald, C. L., Hurtmans, D., Ngadi, Y., Clerbaux, C., et al. (2014). Global distributions, time series and error characterization of atmospheric ammonia (NH_3) from IASI satellite observations. *Atmospheric Chemistry and Physics*, *14*(6), 2905–2922. https://doi.org/10.5194/acp-14-2905-2014

Van Damme, M., Erisman, J. W., Clarisse, L., Dammers, E., Whitburn, S., Clerbaux, C., et al. (2015). Worldwide spatiotemporal atmospheric ammonia (NH_3) columns variability revealed by satellite. *Geophyscial Research Letters*, 1–9. https://doi.org/10.1002/2015GL065496

Van Damme, M., Whitburn, S., Clarisse, L., Clerbaux, C., Hurtmans, D., & Coheur, P. F. (2017). Version 2 of the IASI NH_3 neural network retrieval algorithm: Near-real-time and reanalysed datasets. *Atmospheric Measurement Techniques*, *10*(12), 4905–4914. https://doi.org/10.5194/amt-10-4905-2017

Van Damme, Martin, Clarisse, L., Whitburn, S., Hadji-Lazaro, J., Hurtmans, D., Clerbaux, C., & Coheur, P. F. (2018). Industrial and agricultural ammonia point sources exposed. *Nature*, *564*(7734), 99–103. https://doi.org/10.1038/s41586-018-0747-1

Walker, J. M., Philip, S., Martin, R. V., & Seinfeld, J. H. (2012). Simulation of nitrate, sulfate, and ammonium aerosols over the United States. *Atmospheric Chemistry and Physics*, *12*(22), 11213–11227. https://doi.org/10.5194/acp-12-11213-2012

Warner, J. X., Dickerson, R. R., Wei, Z., Strow, L. L., Wang, Y., & Liang, Q. (2017). Increased atmospheric ammonia over the world's major agricultural areas detected from space. *Geophysical Research Letters*, *44*(6), 2875–2884. https://doi.org/10.1002/2016GL072305

Warner, J. X., Wei, Z., Larrabee Strow, L., Dickerson, R. R., & Nowak, J. B. (2016). The global tropospheric ammonia distribution as seen in the 13-year AIRS measurement record. *Atmospheric Chemistry and Physics*, *16*(8), 5467–5479. https://doi.org/10.5194/acp-16-5467-2016

Whitburn, S., Van Damme, M., Clarisse, L., Bauduin, S., Heald, C. L., Hurtmans, D., et al. (2016). A flexible and robust neural network IASI-NH_3. *Journal of Geophysical Research Atmospheres*, *121*(11), 6581–6599. https://doi.org/10.1002/2016JD024828

Yao, X., & Zhang, L. (2016). Trends in atmospheric ammonia at urban, rural, and remote sites

across North America. *Atmospheric Chemistry and Physics*, *16*(17), 11465–11475. https://doi.org/10.5194/acp-16-11465-2016

Zhang, Y., Moges, S., & Block, P. (2016). Optimal cluster analysis for objective regionalization of seasonal precipitation in regions of high spatial-temporal variability: Application to Western Ethiopia. *Journal of Climate*, *29*(10), 3697-3717. https://doi.org/10.1175/JCLI-D-15-0582.1

Zhu, L., Henze, D. K., Cady-Pereira, K. E., Shephard, M. W., Luo, M., Pinder, R. W., et al. (2013). Constraining U.S. ammonia emissions using TES remote sensing observations and the GEOS-Chem adjoint model. *Journal of Geophysical Research: Atmospheres*, *118*(8), 3355–3368. https://doi.org/10.1002/jgrd.50166

NH₃ column (10¹⁶ molec/cm²)

NH$_3$ column (10^{16} molec/cm^2)